

# L- and M-band imaging observations of the Galactic Center region

T. Viehmann<sup>1</sup>, A. Eckart<sup>1</sup>, R. Schödel<sup>1</sup>, J. Moustaka<sup>1</sup>, C. Straubmeier<sup>1</sup>, and J.-U. Pott<sup>1,2</sup>

<sup>1</sup> I. Physikalisches Institut, Universität zu Köln, Zülpicher Str. 77, D-50937 Köln, Germany

<sup>2</sup> ESO, Karl-Schwarzschild-Str. 2, D-85748 Garching, Germany

Received ; Accepted

**Abstract.** In this paper we present near-infrared  $H$ -,  $K$ -,  $L$ - and  $M$ -band photometry of the Galactic Center from images obtained at the ESO VLT in May and August 2002, using the NAOS/CONICA ( $H$  and  $K$ ) and the ISAAC ( $L$  and  $M$ ) instruments\*. The large field of view ( $70'' \times 70''$ ) of the ISAAC instrument and the large number of sources identified ( $L - M$  data for a total of 541 sources) allows us to investigate their colors, infrared excesses and the extended dust emission. Our new  $L$ -band magnitude calibration reveals an important offset to the traditionally used “standard” calibrations, which we attribute to the use of the variable star IRS 7 as a flux calibrator. Together with new results on the extinction towards the Galactic Center (Scoville et al. 2003; Raab 2000), our magnitude calibration results in stellar color properties expected from standard stars and removes any necessity to modify the  $K$ -band extinction. The large number of sources for which we have obtained  $L - M$  colors allows us to measure the  $M$ -band extinction to  $A_M = (0.056 \pm 0.006)A_V$ , i.e.  $A_M \approx A_L$ , a considerably higher value than what has so far been assumed.  $L - M$  color data has not been investigated previously, due to lack of useful  $M$ -band data. We find that this color is a useful diagnostic tool for the preliminary identification of stellar types, since hot and cool stars show a fairly clear  $L - M$  color separation, with average  $L - M$  colors of  $0.46 \pm 0.17$  for emission-line stars and  $-0.05 \pm 0.27$  for cool red giants/AGB stars. This is especially important if visual colors are not available, as in the Galactic Center.

For one of the most prominent dust embedded sources, IRS 3, we find extended  $L$ - and  $M$ -band continuum emission with a characteristic bow-shock shape. An explanation for this unusual appearance is that IRS 3 consists of a massive, hot, young mass-losing star surrounded by an optically thick, extended dust shell, which is pushed northwest by wind from the direction of the IRS 16 cluster and Sgr A\*.

**Key words.** Galactic Center – Infrared – Calibration – Stellar Classification

## 1. Introduction

The Galactic Center stellar cluster shows some intriguing characteristics: it is extremely dense, with an unusual observed stellar population consisting mainly (80% of the  $K \lesssim 14$  stars according to Ott et al. 1999) of late-type red giants, many of which are suspected to lie on the asymptotic giant branch (AGB), as well as young massive stars with energetic winds. Spectroscopic measurements (e.g. Krabbe et al. 1995; Najarro et al. 1997) allow identification of these two components, the late-type red giants and supergiants showing strong  $2.3 \mu\text{m}$  CO bandhead absorption and the massive, hot and windy stars (“He stars”) exhibiting He and H emission lines. The emission line stars appear to dominate energetically in the central few arcseconds, where the bright IRS 16 cluster is located. These stars are generally classi-

fied as Ofpe/WN9, although some of them might be luminous blue variables (LBV) and a few show characteristics of Wolf-Rayet stars. A third, less numerous component of the Galactic Center stellar cluster consists of luminous, extended objects with steep, red and featureless ( $K$ -band) spectra and a strong infrared excess. These sources were considered as potential YSO candidates (Clénet et al. 2001; Ott et al. 1999; Krabbe et al. 1995). Recently, however, they have been successfully described as bow-shock sources (Tanner et al. 2002, 2003; Rigaut et al. 2003; Eckart 2004), with the implication that the stars powering these luminous infrared sources are windy stars of the types mentioned above.

We present multi-band ( $H$ ,  $K$ ,  $L$  and  $M$ ) photometry of the Galactic Center, obtained with the ESO VLT, in order to further investigate the properties of the Galactic Center stellar cluster. The large number of sources available for color analysis allows for improved statistics, resulting in a new  $L$ -band calibration which eliminates anomalous color effects found in other surveys of the Galactic Center stellar cluster (e.g. Clénet et al. 2001; Simons & Becklin 1996). The large field of view ( $70'' \times 70''$ ) of the ISAAC instrument allows us to com-

Send offprint requests to: T. Viehmann, e-mail: viehmann@ph1.uni-koeln.de

\* based on observing run 69.B-0101(A) at the Very Large Telescope (VLT) of the European Southern Observatory (ESO) on Paranal in Chile.

pare the immediate Galactic Center cluster population with the stellar population further out, with separations from SgrA\* of up to about half an arcminute. This comparison results in a confirmation of the new extinction values of Scoville et al. (2003). Previous (multi-band) imaging studies of the Galactic Center, besides being limited in their field of view to e.g.  $13'' \times 13''$  (Clénet et al. 2001; Davidge et al. 1997), appear to have neglected the *M*-band ( $4.66\text{ }\mu\text{m}$ ), which shows some interesting properties, which we discuss in this paper.

## 2. Observations and data reduction

### 2.1. ISAAC observations

On May 23rd – 30th 2002, *L*- and *M*-band ( $3.78\text{ }\mu\text{m}$  and  $4.66\text{ }\mu\text{m}$ ) imaging observations of the Galactic Center were obtained with the ISAAC infrared imager at the ESO VLT (Unit Telescope 1, Antu), as part of a joint IR/X-ray monitoring program of Sgr A\* (Eckart et al. 2003b; Baganoff et al. 2003). The seeing-limited images were taken in ISAAC's higher resolution mode, with a pixel scale of  $0.071''$  and a field of view of  $72.6'' \times 72.6''$  (see Cuby et al. 2002). Seeing conditions varied during the campaign, resulting in angular resolutions between  $0.4''$  and  $1.2''$ . The observations were made in batches of 25 to 40 pairs of frames (with chopping and nodding), with an integration time of 0.99 s per frame.

### 2.2. NAOS/CONICA observations

During the science verification phase of the commissioning and observatory preparation of the NAOS/CONICA adaptive optics assisted imager/spectrometer at the ESO VLT (UT4, Yepun), *H*- and *K<sub>s</sub>*-band ( $1.6\text{ }\mu\text{m}$  and  $2.1\text{ }\mu\text{m}$ ) images of the Galactic Center were obtained on 30 August 2002, with a FWHM of 43 and 56 mas, respectively, and a pixel scale of  $0.0132''/\text{pixel}$  (Schödel et al. 2002, 2003). The total integration times were 1500 s and 1200 s, respectively. Since the  $K - K_s$  color difference is an order of magnitude smaller than the photometric accuracy that we reach, no further distinction between *K* ( $2.2\text{ }\mu\text{m}$ ) and *K<sub>s</sub>* will be made in this paper. Since the purpose of the NAOS/CONICA images in this context was to gain additional color information for analysing the seeing-limited ISAAC *L*- and *M*-band images, the pixel scale of the NAOS/CONICA images was reduced to the corresponding  $0.071''/\text{pixel}$  via re-binning. Further data reduction was then performed using the same methods as with the ISAAC images.

### 2.3. Data reduction

All image processing was performed using routines from the IRAF software package. The data reduction procedures employed were standard: After flat field correction, the paired images were subtracted from each other and subsequently shifted to a common reference frame. All such subtracted images from each batch were then combined by calculating the median, which also effectively removed cosmic rays and bad pixels. The final images were then created by coaddition of the median images with the best effective seeing, i.e. better than  $0.6''$ ,

resulting in total integration times of 229.7 s for the *L*-band image and 162.4 s for the *M*-band image. The final *M*-band image is shown in Fig. 1. Finally, PSF-fitting photometry was performed on all four final images using the IRAF/DAOPHOT software package.

## 2.4. Photometry

The observing conditions for both the ISAAC and the NAOS/CONICA observations were generally photometric and are adequate for relative photometry. For the *L*- and *M*-band case, we linked the calibration of the IRAF/DAOPHOT PSF-fitting results to observed flux density reference stars. For the *H*- and *K*-band, we relied on data taken from the literature (Clénet et al. 2001; Depoy 1990).

### *L*- and *M*-Band Magnitude Calibration

For calibration purposes, the standard stars HD 130163 ( $m_L = 6.856$ ,  $m_L - m_M \approx 0$ , van der Blieck et al. 1996) and HR 5249 ( $m_M = 4.53$ , van der Blieck et al. 1996) were imaged together with science observations on May 28th 2002, using identical techniques. The airmass difference was small (maximum 0.2), resulting in corrections smaller than 0.04 magnitudes, which are insignificant given the uncertainties in the photometry (see section 3.1). These observations were used to calibrate the final *L*- and *M*-band images, using aperture photometry on approximately 30 isolated stars.

### *K*-Band Magnitude Calibration

Reference *K*-band magnitudes for some of the bright IRS sources were taken from Clénet et al. (2001), who fixed their zero-point with the photometry of Ott et al. (1999). The differences between the DAOPHOT magnitudes and the values of Clénet et al. (2001) were averaged, resulting in a calibration value which was subtracted from the DAOPHOT magnitudes. Saturated sources were excluded from the determination of the calibration magnitudes.

### *H*-Band Magnitude Calibration

The main problem encountered in calibrating the *H*-band data was saturation. All the bright *H*-band sources (for which magnitudes are available) are saturated in the NAOS/CONICA image, whereas no magnitudes for the weaker unsaturated sources could be found in the literature.

The solution employed here was secondary calibration using an *H*-band mosaic made from images taken with the SHARP speckle imager in 1992 (Eckart et al. 1992). This image was flux calibrated using data for the brighter IRS sources (Depoy 1990). Subsequently, the NAOS/CONICA image was calibrated with the flux densities from weaker, isolated (i.e. clearly separated from their neighbors) sources in the SHARP mosaic image.

The total uncertainty of the photometry results is estimated as 0.25 magnitudes in the *H*- and *K*-band and 0.15 magnitudes in the *L*- and *M*-band. The difference is due to the different

calibration procedures and the different shape of the respective PSFs of the ISAAC and NAOS/CONICA images, resulting in less accurate fit results for the latter. The limiting magnitudes of this analysis are 12.73 (*M*-band), 14.47 (*L*-band), 17.66 (*K*-band) and 20.34 (*H*-band).

### 2.5. Additional data

The field of view of the NAOS/CONICA images (approximately  $17.8'' \times 17.8''$ ) is much smaller than the ISAAC field of view. In order to check the properties of sources outside this region, additional *H*- and *K*-band images were analysed.

#### ISAAC *K*-band image

During the 1999 ISAAC spectroscopy campaign (Eckart et al. 1999), a *K*-band image of the Galactic Center was obtained, using ISAAC's lower resolution mode (pixel scale  $0.148''$ , field of view approximately  $150'' \times 150''$ , see Cuby et al. 2002).

#### Gemini data

For *H*-band, we also used publicly released Gemini data from the 2000 Galactic Center Demonstration Science Data Set (using the Quirc camera and the Hokupa'a adaptive optics system, see Cotera & Rigaut 2001).

In order to limit the amount of work required, photometry on these datasets was performed only for the brighter sources in the *L*-band image ( $m_L < 9.5$ ) and an exemplary selection of approximately 15 fainter sources in order to verify that the faint stars do not show systematically different color properties than the bright stars. The images were calibrated relative to our NAOS/CONICA data.

## 3. Results

### 3.1. Photometry

Table 1 summarizes the photometry of those sources within the NAOS/CONICA field of view ( $17.8'' \times 17.8''$ ) that are detectable in at least one of the ISAAC images. Table 2 summarizes the photometry of the sources outside the NAOS/CONICA field of view, for which therefore only *L*- and *M*-band data are available.

Notes:

- The named sources are identified in Fig. 2.
- The position offset is given in arcseconds relative to IRS 16NE. In order to calculate the position offsets with respect to the location of the infrared/radio source Sgr A\* (Reid et al. 2002; Schödel et al. 2003), one has to add  $2.83''$  in right ascension and  $-0.91''$  in declination. Given the larger field of view, the positions were derived from our best seeing L-band map and aligned with respect to the radio positional reference frame for the Galactic Center as given by Reid et al. (2002).
- For the astrometry, the pixel scale from the ISAAC user manual was used (see Cuby et al. 2002) with minor corrections based on the comparison of our positions to those

of Ott et al. (1999). From this comparison, we estimate the absolute position error as approximately 0.09 arcseconds. Relative positions in our images can be derived with a much higher precision of at least half a pixel, i.e.  $\lesssim 0.035''$ .

- If a source was not detected at a given wavelength, the maximum detected magnitude in that band is given as a lower limit (i.e. upper brightness limit). These cases were excluded from the corresponding color-color diagrams.

### 3.2. New *L*-band calibration

Since our *L*-band calibration introduces an offset of approximately 0.5 mag to the frequently used calibration of Blum et al. (1996), some comments are necessary.

Calibrating the *L*-band image with reference magnitudes taken from Clénet et al. (2001), as for the NAOS/CONICA *K*-band image (see section 2.4), resulted in  $(K-L)_{\text{obs}}$  colors which were *at least* 0.3 magnitudes too blue. An examination of the color-color-diagrams showed this effect to be systematic, since *the whole population* was blueshifted in  $K - L$ , whereas the  $H - K$  colors lie within the expected range for stellar sources. It therefore seems unlikely that the *K*-band calibration is wrong, especially considering that it is based on stars shown to be non-variable (Ott et al. 1999; Clénet et al. 2001). Directly calibrating the *L*-band image with the observed calibration star instead of adjusting the zero-point with already published photometry does not show this effect. We note that Clénet et al. (2001) also found unusually blue  $K - L$  values, which they attributed to a lower *K*-band extinction. If the extinction law remains unchanged, this implicitly suggests a lower extinction  $A_V$ , which our observations can confirm (see section 3.3).

The *L*-band data and thus the calibration given by Blum et al. (1996) are taken from Depoy & Sharp (1991). Their calibration (which is not discussed in detail in their 1991 publication) was fixed with the star IRS 7, for which Blum et al. (1996); Tamura et al. (1996) and Ott et al. (1999) have shown that it is variable with an amplitude of approximately 1 mag in *K*-band. It seems that the offset to the other frequently applied calibration by Simons & Becklin (1996) is also due to their use of the variable source IRS 7 as flux calibrator. Our new *L*-band calibration, however, provides a clear improvement to this point, especially since it does not rely on any (non-)variability assumptions for the observed sources and does not result in unexpected  $K - L$  color effects. We finally note that a higher extinction than the assumed  $A_V = 25$  mag would result in even bluer  $K - L$  colors, requiring an even larger offset to the *L*-band calibrations mentioned above.

### 3.3. Colors and extinction

For de-reddening purposes, the extinction law of Rieke & Lebofsky (1985) was adopted, i.e.  $A_H = 0.175A_V$ ,  $A_K = 0.112A_V$ ,  $A_L = 0.058A_V$  and (initially)  $A_M = 0.023A_V$ . Since recent work by Scoville et al. (2003) indicates that the extinction toward the Galactic Center exhibits a broad minimum over the area of the IRS 16 Cluster and the Northern Arm, their value of  $A_V = 25$  mag was assumed, instead of the

traditional average value of  $A_V = 27$  or even 30 mag (Rieke 1987). This choice is supported by the colors of the stars observed, especially  $K - L$  (see section 3.2), since they would otherwise be too blue.

In the  $HKL$  color-color diagram (Fig. 5), the majority of sources form a cluster in the area populated by stars (for intrinsic colors see Koornneef 1983), with a fairly sharp boundary towards bluer colors. This is satisfactory, since the majority of sources exhibit colors that lie in the possible color range for stellar sources. Only *very few* objects show bluer colors, which can be seen as exceptions. Quite a few objects appear to be strongly reddened, especially within the inner area covered by the NAOS/CONICA images. This is not surprising, since the dust and gas of the ‘mini-spiral’ passes through this region.

The conclusion to be drawn here is that the newer findings concerning extinction (Scoville et al. 2003), together with our new *L*-band calibration, provide a consistent picture without requiring modifications of the extinction law at this point.

### 3.3.1. Comparison of outer and inner field

With the exception of some highly reddened sources (e.g. IRS 1W, IRS 3, IRS 10, IRS 21) found almost exclusively within the inner field (i.e. the  $18'' \times 18''$  of the NAOS/CONICA field of view), the stars from the inner and outer regions cluster in the same area of the two-color diagrams, with the clustering much more pronounced for the stars from the outer region. The highly reddened sources from the inner field are apparently obscured/reddened by gas and dust from the mini-spiral (either directly or by a bow-shock type interaction).

The  $H - K$  and  $K - L$  colors obtained from our data, especially if one excludes unusual stars such as Wolf-Rayet stars etc., confirm the results of Scoville et al. (2003) for the lower extinction (we assumed  $A_V=25$  mag) towards the IRS 16 cluster and the Northern Arm of the mini-spiral, since the colors – after dereddening – agree with the intrinsic colors of stars given by Koornneef (1983). Any higher extinction would lead to significantly bluer intrinsic colors, which cannot be explained in a straightforward manner. Our data indicates that this relatively low extinction applies to the complete region covered by the (high-resolution) ISAAC images, i.e. the inner  $70'' \times 70''$ . This can be inferred from the two-color diagrams (Figs. 5 and 6), since the populations of the inner and outer region cluster in the same area of these diagrams. If the extinction were to increase significantly within the ISAAC high resolution field of view, the ‘outer’ population (or at least a significant part of it) should show systematically redder colors than the main part of the ‘inner’ population, which is clearly not the case. The higher extinctions of 35 to 50 mag reported by Scoville et al. (2003) thus apply to areas outside the inner 70 arcseconds, which is consistent with the location of the circum-nuclear molecular ring, which has a sharp inner edge (Latvakoski et al. 1999).

### 3.3.2. Extinction in *M*-band

Our *M*-band calibration, using two calibration stars of significantly different magnitude (see section 2.4), provides rather surprising results: the stars appear too blue by about 0.7 mag in  $L - M$ , if one applies the reddening law of Rieke & Lebofsky (1985), i.e.  $A_M=0.023A_V$ . However, the ISO/SWS Galactic Center extinction measurements of Lutz et al. (1996) and Lutz (1999), while generally in agreement with the extinction law of Rieke & Lebofsky (1985), permit considerably higher (or lower) extinctions in the  $4-5 \mu\text{m}$  regime within their uncertainties. This is especially true if one considers that their extinction values increase again longward of  $5 \mu\text{m}$  (see also Raab 2000). Visual inspection of the distribution of  $L - M$  colors in the color-color diagram (Fig. 6) suggests that  $A_M \approx A_L$ , since the bulk of the  $L - M$  colors observed then agree with the expected  $L - M$  colors for stellar sources (Koornneef 1983).

Our extensive  $L - M$  color data available for a total of 541 sources allows us to quantify the *M*-band extinction more precisely, assuming that the theoretical intrinsic colors given by Koornneef (1983) are valid. From the mean observed and theoretical intrinsic  $L - M$  colors averaged over all types of stars we can calculate the *M*-band extinction via:

$$\frac{A_M}{A_V} = \frac{1}{A_V}((L - M)_{\text{Koornneef}} - (L - M)_{\text{obs}} + A_L) = 0.056 \pm 0.006.$$

Here we quote a  $3\sigma$  uncertainty. This result is plotted in Fig. 7 and agrees very well with the above estimate of  $A_M \approx A_L$ , with  $A_L=0.058A_V$  following Rieke & Lebofsky (1985). The possible luminosity-induced bias (observed stars are bright) is  $< 0.003$  and therefore not significant given the uncertainties.

Assuming for simplicity a Gaussian distribution of the  $L - M$  values for simplicity, we find a corresponding standard deviation of  $\sigma_{L-M}=0.51$ , which allows the calculation of the contribution  $\sigma_{\text{ext}}$  of screening and source intrinsic effects to the  $L - M$  distribution. The uncertainties of the distribution are given by

$$\sigma_{L-M}^2 = \sigma_L^2 + \sigma_M^2 + \sigma_{\text{Koornneef}}^2 + \sigma_{\text{ext}}^2,$$

where  $\sigma_{\text{Koornneef}}=0.16$  represents the scattering of theoretical intrinsic colors over the whole range of stellar types as listed by Koornneef (1983). Here  $\sigma_L$  and  $\sigma_M$  are the uncertainties in the *L*-and *M*-band magnitudes. We find  $\sigma_{\text{ext}}=0.44$ , which implies that the *main* contribution to the width of the  $L - M$  color distribution is due to screening effects and source-intrinsic reddening (i.e. local dust concentrations etc.). The main caveat here is that the  $L - M$  color distribution is not Gaussian (there are two principal stellar types with different intrinsic colors, i.e. red giants and young, massive emission-line stars). However, the width of the distribution due to different stellar type components is considerably smaller than the scattering observed. Nevertheless, this analysis is useful as a preliminary estimate, and further *M*-band studies of the Galactic Center are necessary to clarify the situation.

### 3.3.3. Colors of He-stars and red giants

A comparison of the  $L - M$  colors of the named sources of known type (i.e. He-stars or cool red giants/AGB) shows a

fairly clear color separation, with the cool stars significantly *bluer* (see Table 1 and Fig. 6). This result is in general agreement with the colors given by Koornneef (1983): Hot stars have on average an  $(L - M)_{\text{intrinsic}}$  of  $\approx -0.05$ , while cool giants have  $(L - M)_{\text{intrinsic}}$  values of typically -0.2 to -0.3. In our sample, the average observed  $(L - M)_{\text{obs}}$  values are  $0.46 \pm 0.17$  for the emission-line stars and  $-0.05 \pm 0.27$  for the cool stars (ten of each, see Table 1), with the standard deviation as uncertainty. Therefore, the  $L - M$  color, and more particularly the  $H - K$  versus  $L - M$  color-color diagram is a reasonably good diagnostic tool for preliminary identification of these stellar types. Applying this  $L - M$  criterion to our sample, we find that the emission-line stars show a clear concentration in the inner region, with only about ten emission-line-star candidates in the area outside the  $18'' \times 18''$  NAOS/CONICA field of view (containing 166 objects with full photometry data), as opposed to at least forty such objects in the inner region (197 objects in total).

$K - L$  colors are much less useful in this context, since the  $K - L$  color separation is comparatively low. Naturally, spectroscopic evidence is required for a definite classification.

An additional comment can be made on the dereddened (i.e. intrinsic)  $(K - L)_{\text{intrinsic}}$  and  $(L - M)_{\text{intrinsic}}$  colors of the He-stars. These appear to be slightly but systematically redder ( $\approx 0.2$  mag) than expected for hot stars, whose  $(K - L)_{\text{intrinsic}}$  and  $(L - M)_{\text{intrinsic}}$  colors are approximately 0 to -0.1. This indicates the presence of an infrared excess. A possible explanation for such an excess could be that the He-stars all show signs of an interaction with the dusty Galactic Center ISM. This excess could be of a similar nature but much less pronounced than the bow shock sources along the mini-spiral (Tanner et al. 2002, 2003; Rigaut et al. 2003; Eckart 2004; Clénet et al. 2004). Our result is in general agreement with the findings of Davidge et al. (1997), who indicate that the  $K - L$  colors of the He-stars are clearly redder than those of known emission line stars in the LMC.

### 3.4. IRS 3

One of the most intriguing mid-infrared sources in the Galactic Center region is IRS 3. In the *L*- and *M*-band, this is the most extended source observed here, and also one of the brightest ( $m_M = 3.4$ ). It is much fainter in the *K*-band, hardly visible in the *H*-band ( $m_K = 10.6$ ,  $m_H = 15.0$ ), and also hardly extended at these shorter wavelengths (see Figs. 3 and 4). Consequently, IRS 3 appears to be dominated by dust emission. According to Krabbe et al. (1995), IRS 3 has an almost featureless, red continuum *K*-band spectrum. Also IRS 3 emits strongly at  $10 \mu\text{m}$  (e.g. Gezari et al. 1985).

In our analysis, the *M*-band photocenter of IRS 3 is shifted to the northwest by  $\sim 0.16''$  with respect to the *H*-, *K*- and *L*-band positions. This angular separation is well above the relative positional uncertainty of  $0.035''$  we estimated above and thus not a mere artifact. A visual inspection of the maps clearly shows, however, that the two sources detected by the PSF-fitting algorithm are not distinct sources, but a consequence of the extended flux density distribution. This shift of the photo-

center of the extended *M*-band emission relative to that at shorter wavelengths, combined with the clearly visible asymmetry of the lower contour lines in the NAOS/CONICA *L*-band image (Fig. 4) results in a bow-shock-like appearance, similar to the sources discussed by Tanner et al. (2003), although less distinct than the remarkable source mentioned by Clénet et al. (2004). The asymmetry is the consequence of a compression of the extended emission at its southern edge, resulting in a steeper flux density gradient (“bunched” contour lines). A possible explanation for this unusual appearance is that IRS 3 consists of a hot mass-losing star, e.g. a young, dust-embedded O star (Krabbe et al. 1995) or a dusty protostar or Wolf-Rayet star (Tanner et al. 2003; Horrobin et al. 2004), surrounded by a very thick, extended dust shell, which is pushed northwest by wind from the direction of the IRS 16 cluster and Sgr A\*. Gezari et al. (1985) give a temperature of  $\approx 400$  K for this strong *L*-band source. The *H*- and *K*-band emission is dominated by the stellar source and therefore not extended. The dust shell must be very thick, however, since IRS 3 is a faint source in *K* and especially *H*. The shift in the *M*-band emission is due to part of the dust shell being extended to the northwest. It should be possible to clarify the nature of IRS 3 through *L*- and *M*-band (and possibly longer wavelength) studies at higher resolution, i.e. using adaptive optics or interferometric methods that are becoming available in the infrared (e.g. VLTI or the upcoming LBT, see Eckart et al. 2003a).

## 4. Conclusion

We have presented multi-band infrared photometry of the Galactic Center, covering the large field of view ( $70'' \times 70''$ ) of the ISAAC instrument at the VLT. Our independent *L*-band magnitude calibration, relying on the robust method of observing standard calibration stars, reveals an offset to the traditionally used “standard” calibrations (Depoy & Sharp 1991; Blum et al. 1996; Simons & Becklin 1996). We attribute this offset to the use of the variable star IRS 7 (Blum et al. 1996; Tamura et al. 1996; Ott et al. 1999) as a flux calibrator. This offset is important when investigating colors.

Together with new results on the extinction towards the Galactic Center (Scoville et al. 2003), our magnitude calibration makes the stars redder in  $K - L$ , which results in normal stellar properties. There is no longer any necessity to modify the *K*-band extinction in order to explain strange blue colors.

Color analysis of our large sample of sources is consistent with the results obtained by Scoville et al. (2003) concerning the extinction towards the Galactic Center, since we can compare the color distributions of sources lying within an inner  $18'' \times 18''$  region with sources located further out, up to the  $70'' \times 70''$  limit of the field of view of the ISAAC camera. This comparison reveals no systematic effects, indicating that the average extinction remains at the lower value of  $A_V = 25$  mag up to the sharp inner edge of the circum-nuclear molecular ring.

Our *M*-band data indicates that the extinction in the *M*-band is higher than predicted by the extinction law of Rieke & Lebofsky (1985). The large number of sources for which we have obtained *L* – *M* colors allows a measurement of the *M*-band extinction, assuming that the intrinsic colors

given by Koornneef (1983) are valid. This measurement gives  $A_M=0.056A_V$ , i.e.  $A_M \approx A_L$ , a considerably higher value compared to what has been assumed so far.

Hot and cool stars show a fairly clear  $L-M$  color separation (Koornneef 1983), with the hotter stars exhibiting *redder* colors. Our results show that the Galactic Center sources follow this behavior, for which the  $H-K$  versus  $L-M$  color-color diagram (if available) is a useful diagnostic tool for preliminary identification of stellar types.

Several sources within the central few arcseconds are dust embedded and show extended *L*- and *M*-band emission. For one of the most prominent dust-embedded sources, IRS 3, we find extended *L*- and *M*-band continuum emission with a characteristic bow-shock-like appearance, including a shifted *M*-band photocenter relative to the other wavelengths. A possible explanation for this unusual appearance is that IRS 3 consists of a massive, hot, young and mass-losing star surrounded by an optically thick, extended dust shell, which interacts with the strong wind from the direction of the IRS 16 cluster and Sgr A\*. As a result of this the dust shell is pushed towards the northwest by this wind.

It would appear that further studies in the few micron wavelength range could add considerably to the knowledge of the properties of the stellar population in the Galactic Center. This is especially true for the *M*-band, since it is a fairly long wavelength that is not completely dominated by dust emission. The stars therefore remain accessible for observation.

**Acknowledgements.** This work was supported in part by the Deutsche Forschungsgemeinschaft (DFG) via grant SFB 494. We are grateful to all members of the NAOS/CONICA team from MPIA/MPE, Meudon/Grenoble Observatories, ONERA, ESO. In particular, we thank N. Ageorges, K. Bickert, W. Brandner, Y. Clénet, E. Gendron, M. Hartung, N. Hubin, C. Lidman, A.-M. Lagrange, A.F.M. Moorwood, C. Röhrl, G. Rousset and J. Spyromilio.

## References

- Baganoff, F. K., Maeda, Y., Morris, M., et al. 2003, ApJ, 591, 891
- Blum, R. D., Sellgren, K., & Depoy, D. L. 1996, ApJ, 470, 864
- Clénet, Y., Rouan, D., Gendron, E., et al. 2004, A&A, 417, L15
- Clénet, Y., Rouan, D., Gendron, E., et al. 2001, A&A, 376, 124
- Cotera, A. & Rigaut, F. 2001, Galactic Center Newsletter, 12, 4
- Cuby, J. G., Lidman, C., Moutou, C., Johnson, R., & Doublier, V. 2002, Very Large Telescope: ISAAC User Manual, European Southern Observatory
- Davidge, T. J., Simons, D. A., Rigaut, F., Doyon, R., & Crampton, D. 1997, AJ, 114, 2586
- Depoy, D. L. 1990, in ASP Conf. Ser. 14: Astrophysics with Infrared Arrays, 219–+
- Depoy, D. L. & Sharp, N. A. 1991, AJ, 101, 1324
- Draine, B. T. 1989, in Infrared Spectroscopy in Astronomy, 93–98
- Eckart, A. 2004, in prep.
- Eckart, A., Bertram, T., Mouawad, N., et al. 2003a, Ap&SS, 286, 269
- Eckart, A., Hofmann, R., Duhoux, P., Genzel, R., & Drapatz, S. 1992, in High-Resolution Imaging by Interferometry, 175–+
- Eckart, A., Moulakal, J., Viehmann, T., et al. 2003b, in Astron. Nachr.324, S1: Supplement: Proceedings of the Galactic Center Workshop 2002 - The central 300 parsecs of the Milky Way, 557–561
- Eckart, A., Ott, T., & Genzel, R. 1999, A&A, 352, L22
- Gezari, D. Y., Shu, P., Lamb, G., et al. 1985, ApJ, 299, 1007
- Horrobin, M., Eisenhauer, F., Tecza, M., et al. 2004, Astronomische Nachrichten, 325, 88
- Koornneef, J. 1983, A&A, 128, 84
- Krabbe, A., Genzel, R., Eckart, A., et al. 1995, ApJ, 447, L95+
- Latvakoski, H. M., Stacey, G. J., Gull, G. E., & Hayward, T. L. 1999, ApJ, 511, 761
- Lutz, D. 1999, in ESA SP-427: The Universe as Seen by ISO, 623–+
- Lutz, D., Feuchtgruber, H., Genzel, R., et al. 1996, A&A, 315, L269
- Najarro, F., Krabbe, A., Genzel, R., et al. 1997, A&A, 325, 700
- Ott, T., Eckart, A., & Genzel, R. 1999, ApJ, 523, 248
- Raab, W. 2000, PhD thesis, Ludwig-Maximilians-Universität München, Germany
- Reid, M. J., Menten, K. M., Genzel, R., et al. 2002, ArXiv Astrophysics e-prints
- Rieke, G. H. & Lebofsky, M. J. 1985, ApJ, 288, 618
- Rieke, M. J. 1987, in Nearly Normal Galaxies. From the Planck Time to the Present, 90–95
- Rigaut, F., Geballe, T. R., Roy, J.-R., & Draine, B. T. 2003, in Astron. Nachr.324, S1: Supplement: Proceedings of the Galactic Center Workshop 2002 - The central 300 parsecs of the Milky Way, 551–555
- Schödel, R., Ott, T., Genzel, R., et al. 2003, ApJ, 596, 1015
- Schödel, R., Ott, T., Genzel, R., et al. 2002, Nature, 419, 694
- Scoville, N. Z., Stolovy, S. R., Rieke, M., Christopher, M., & Yusef-Zadeh, F. 2003, ApJ, 594, 294
- Simons, D. A. & Becklin, E. E. 1996, AJ, 111, 1908
- Tamura, M., Werner, M. W., Becklin, E. E., & Phinney, E. S. 1996, ApJ, 467, 645
- Tanner, A., Ghez, A. M., Morris, M., et al. 2002, ApJ, 575, 860
- Tanner, A. M., Ghez, A. M., Morris, M., & Becklin, E. E. 2003, in Astron. Nachr.324, S1: Supplement: Proceedings of the Galactic Center Workshop 2002 - The central 300 parsecs of the Milky Way, 597–603
- van der Bliek, N. S., Manfroid, J., & Bouchet, P. 1996, VizieR Online Data Catalog, 411, 90547

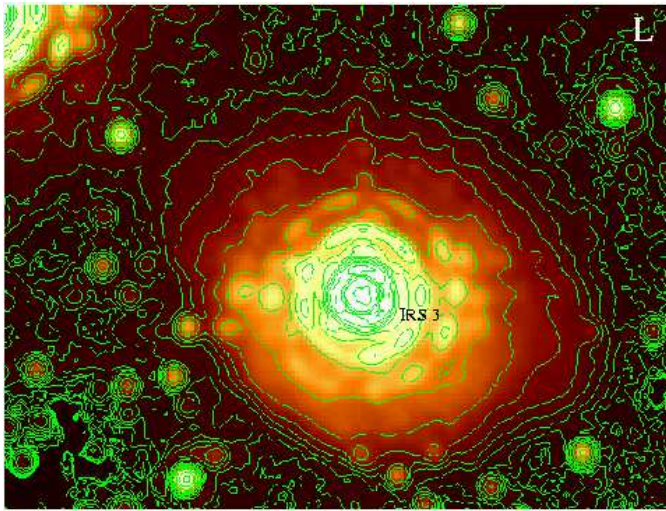


**Fig. 4.** *L*-band view of IRS 3 with NAOS/CONICA (Eckart 2004). The circular structures surrounding the bright sources are due to the adaptive optics. Note the asymmetry in the lower contour lines producing a bow-shock-like effect at the southern edge of the extended emission.

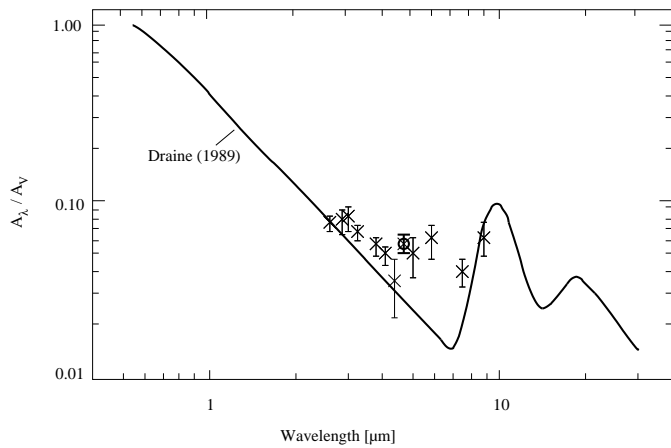


**Fig. 7.** Extinction towards Sgr A\* according to Lutz et al. (1996). The data points are derived from SWS H recombination line data, while the solid curve is the extinction law of Draine (1989) for standard graphite-silicate mixes. The marked data point is our new *M*-band result.

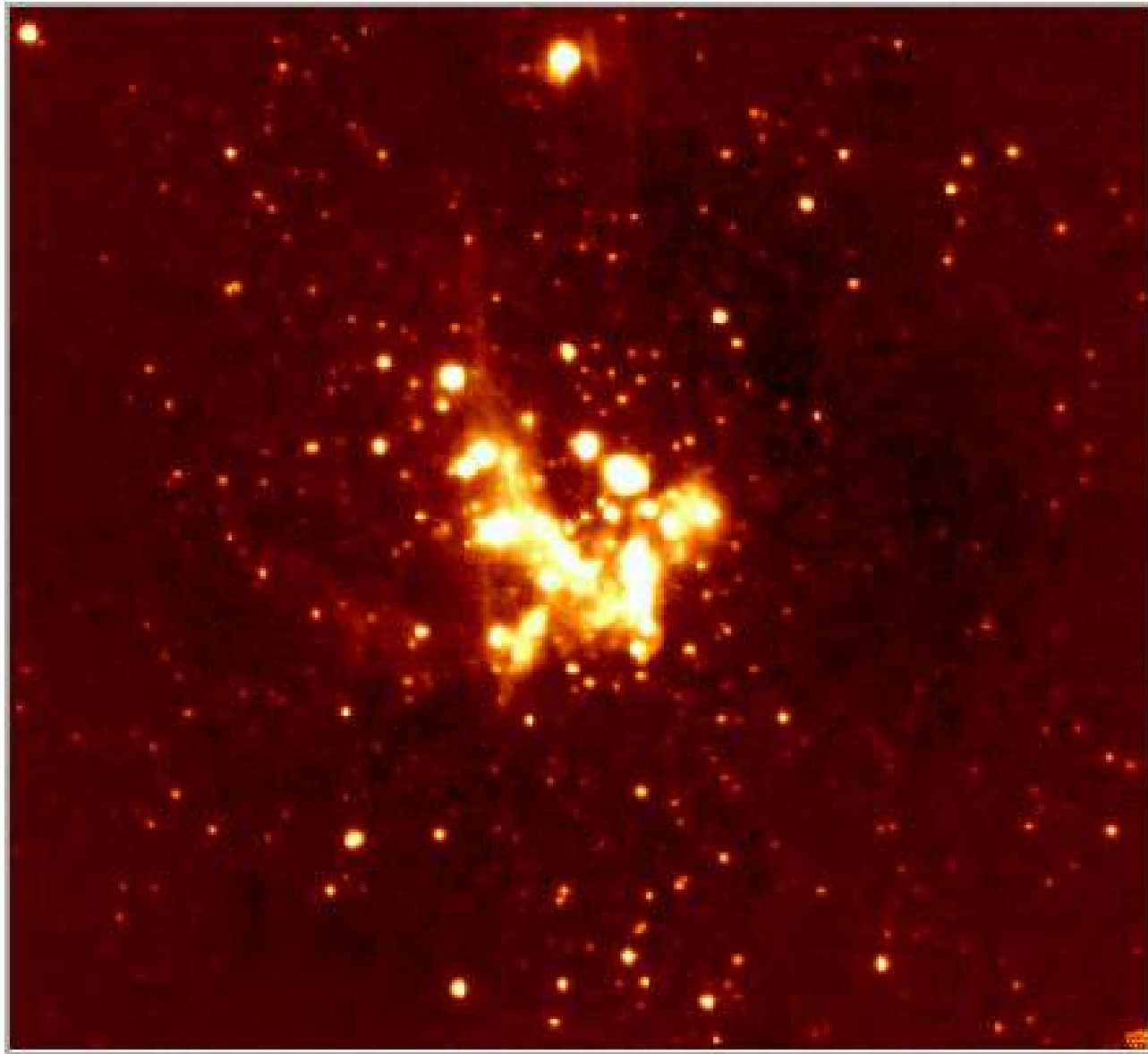


**Fig. 1.** ISAAC *M*-band final image of the Galactic Center. The field of view is 72.6'' $\times$ 72.6''.

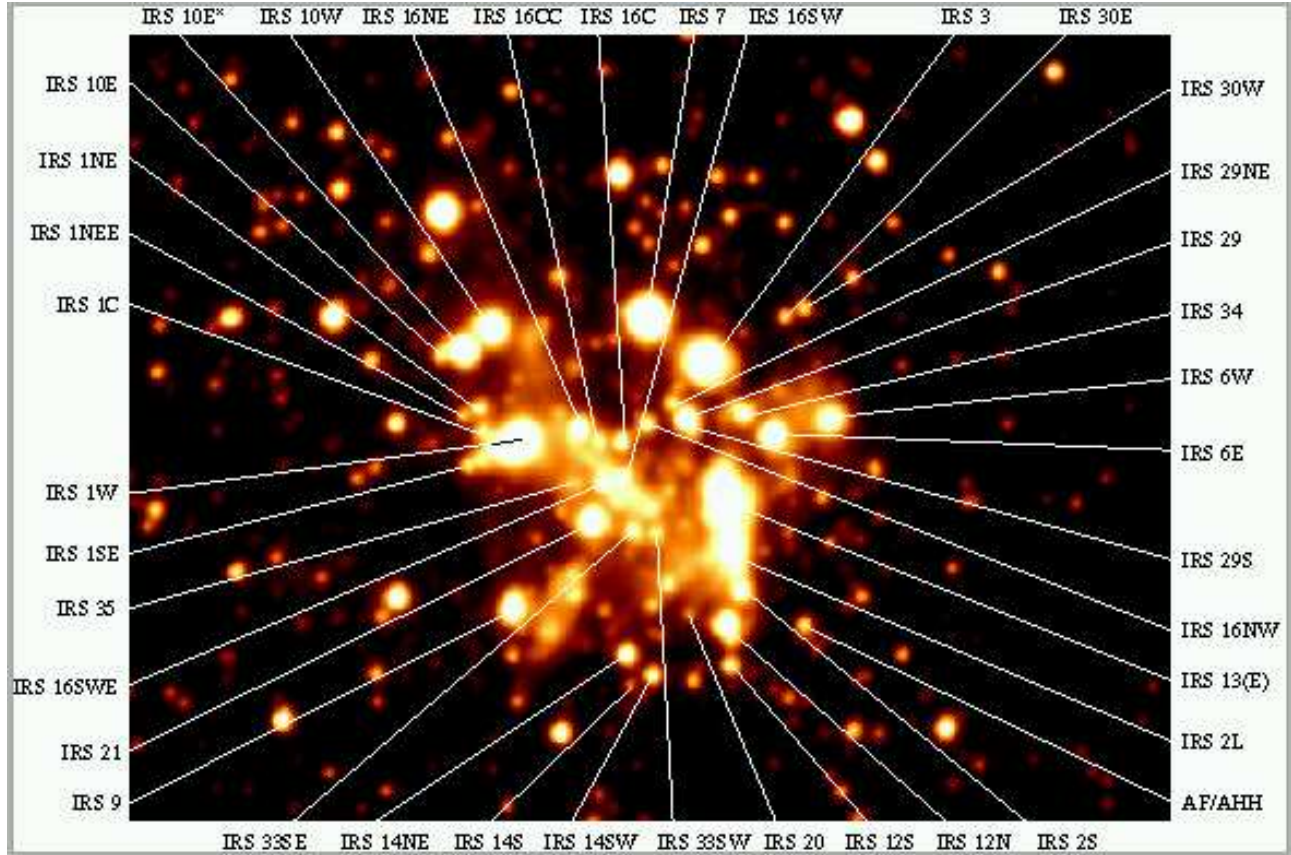


**Fig. 2.** Part of the ISAAC *L*-band final image of the Galactic Center showing most of the named sources.

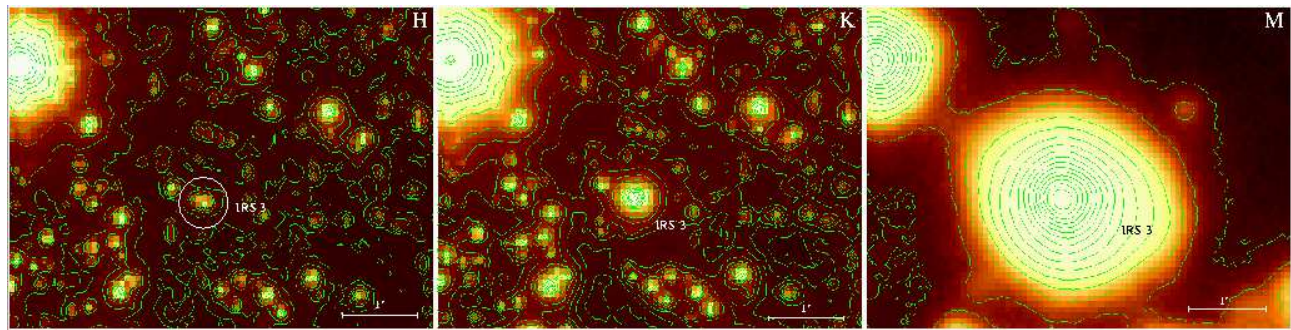


**Fig. 3.** *H*-, *K*- and *M*-band view of IRS 3 (encircled in the *H*-band view). The bright source to the northeast (upper left) is the supergiant IRS 7. A histogram equalization color scale is used, while the contour lines follow a logarithmic scale in order to show the IRS 3 source structure as clearly as possible.

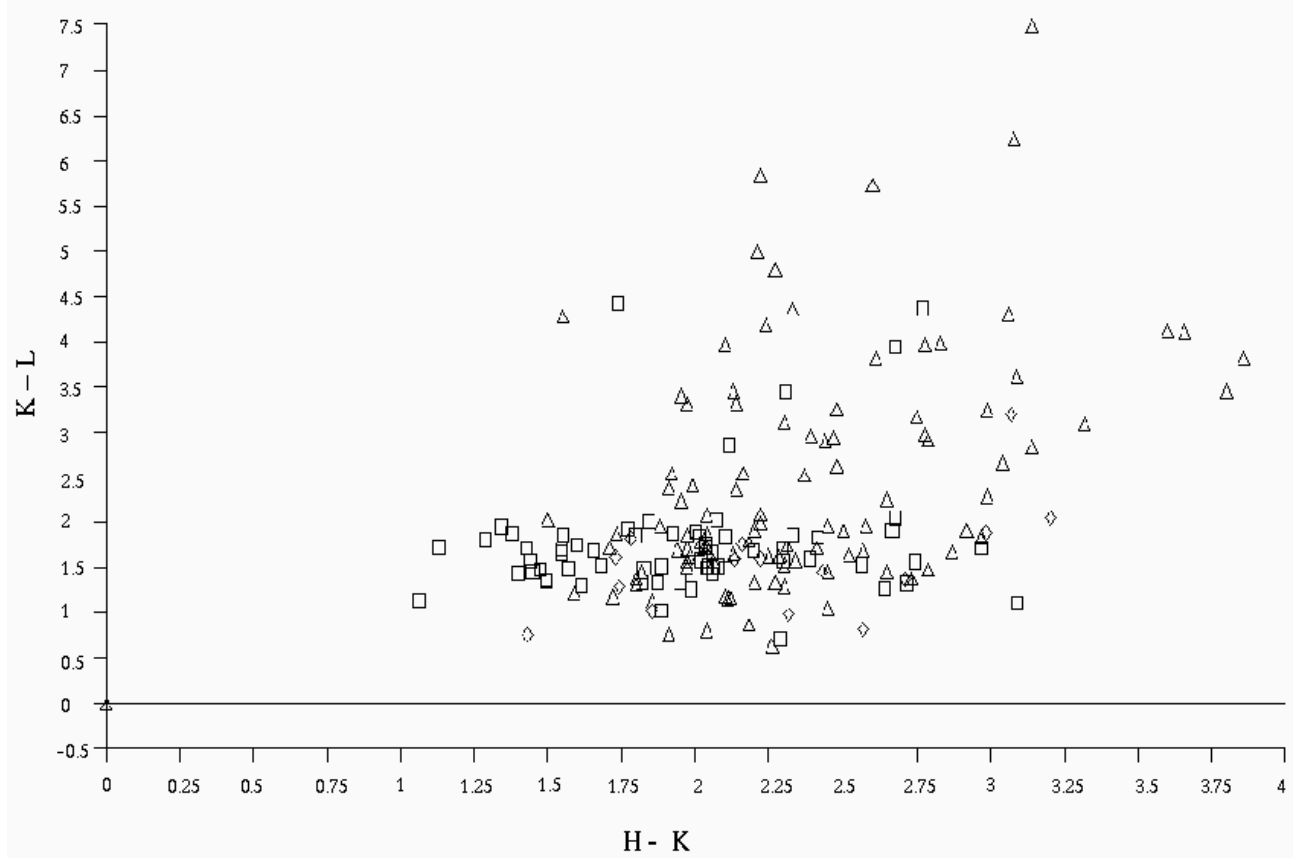


**Fig. 5.** Two-color diagram showing  $(K - L)_{\text{obs}}$  versus  $(H - K)_{\text{obs}}$ . The triangles represent sources from the inner  $18'' \times 18''$ , the squares represent brighter sources ( $m_L < 9.5$ ) and the diamonds a selection of fainter sources from outside this inner region.

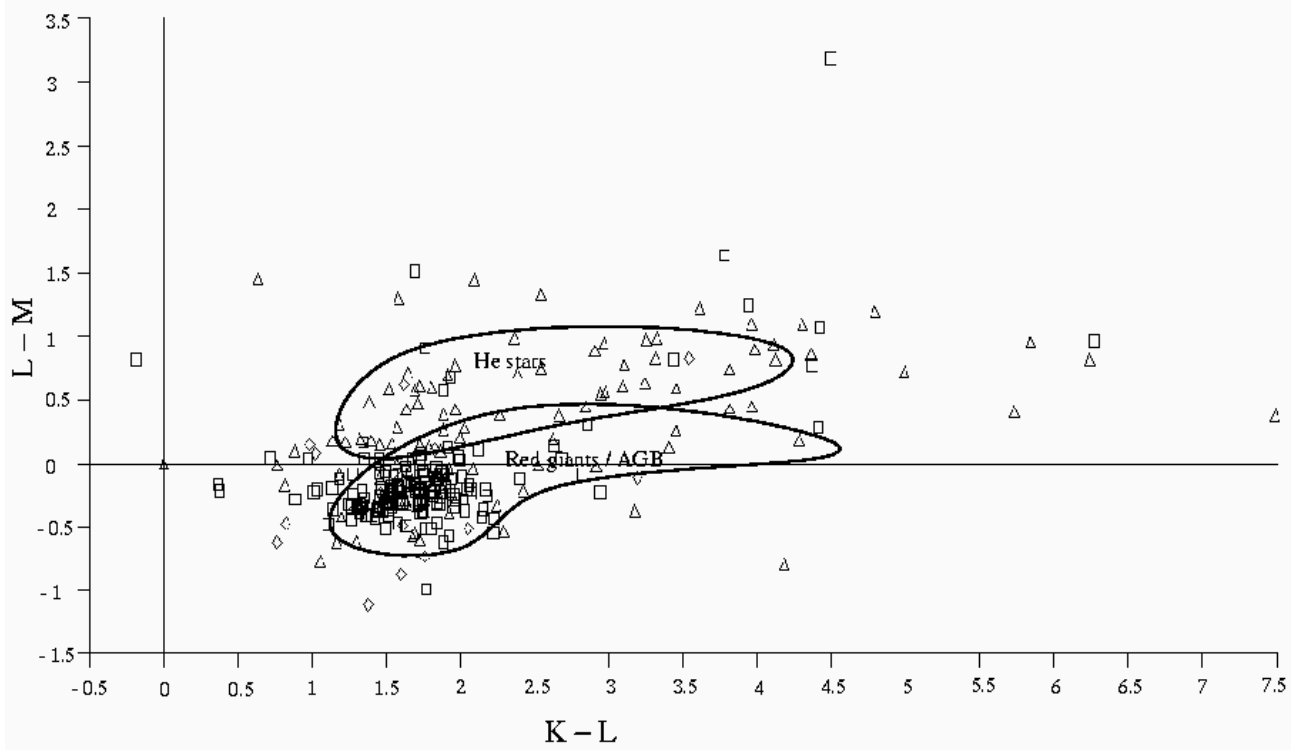


**Fig. 6.** Two-color diagram showing  $(L - M)_{\text{obs}}$  versus  $(K - L)_{\text{obs}}$ . The triangles represent sources from the inner  $18'' \times 18''$ , the squares represent brighter sources ( $m_L < 9.5$ ) and the diamonds a selection of fainter sources from outside this inner region. The marked areas fully contain the spectroscopically identified He stars and red giants / AGB stars from Table 1.

# Online Material

Table 1: Photometry of sources detected in NAOS/CONICA and at least one ISAAC image. The classifications are from Blum et al. (1996), with “cool” referring to red giants or supergiants and “red” signifying objects with featureless *K*-band spectra and a strong IR excess. The zeropoint for the positions is 17:45:42.93 RA -29:00:29.91 DEC (IRS 16NE) in the J2000 coordinate system, with an offset of 2.83''(RA) and -0.91''(DEC) from Sgr A\*.

ID	Name	$\Delta\alpha(^{\circ})$	$\Delta\delta(^{\circ})$	<i>H</i>	<i>K</i>	<i>L</i>	<i>M</i>	$(H - K)_{\text{obs}}$	$(K - L)_{\text{obs}}$	$(L - M)_{\text{obs}}$	Notes
50	IRS 30E	-8.59	4.81	13.12	10.33	8.84	9.12	2.80	1.48	-0.28	
102	IRS 9	2.67	-7.51	11.78	9.41	6.89	6.90	2.38	2.52	-0.02	
179		-0.56	-1.25	14.54	12.40	9.08	8.09	2.14	3.32	0.99	
181	IRS 30W	-9.40	5.17	12.86	10.21	8.76	8.87	2.65	1.45	-0.12	
187	IRS 29	-4.51	0.50	14.16	10.36	6.90	6.31	3.81	3.45	0.59	WC9
197		1.69	-4.53	13.15	11.30	10.17	9.99	1.85	1.13	0.18	
200		-7.53	-9.83	14.46	12.09	10.65	>12.73	2.37	1.44	-3.08	
202	IRS 14SW	-3.33	-10.02	11.83	9.56	8.23	8.54	2.27	1.33	-0.31	cool
277	IRS 16C	-1.79	-0.49	11.70	9.64	8.07	7.78	2.06	1.57	0.29	He I
373		-11.42	6.48	13.02	>17.66	8.97	9.24	-5.64	9.69	-0.27	
376		-1.45	-2.44	13.76	10.84	8.92	8.23	2.92	1.92	0.69	
382		0.04	-6.83	>20.34	14.21	8.35	7.70	7.13	5.86	0.65	
383	IRS 12N	-6.38	-7.87	11.73	9.25	6.63	6.43	2.48	2.63	0.19	cool
385	IRS 14S	-2.37	-10.44	13.02	10.90	9.71	9.80	2.12	1.18	-0.08	
417		-6.82	4.09	14.25	11.73	10.08	9.37	2.52	1.65	0.72	
418	IRS 16CC	-0.87	-0.49	12.13	10.19	8.50	7.92	1.94	1.69	0.57	He I
421		0.28	5.28	14.66	11.99	10.65	>12.73	2.66	1.34	-3.08	
422		3.23	5.90	15.06	12.59	10.89	>12.73	2.47	1.70	-2.84	
423	IRS 10E	5.87	2.97	12.63	10.50	8.84	8.92	2.13	1.65	-0.08	cool
426		-10.01	2.82	14.28	12.02	11.39	9.93	2.26	0.63	1.46	
427		0.70	-3.38	13.41	10.90	9.58	>12.73	2.50	1.32	-4.15	
428	IRS 16NW	-2.86	0.26	11.66	9.84	8.38	8.24	1.82	1.46	0.14	He I
430	IRS 29S	-4.82	0.01	12.33	10.34	9.81	>12.73	2.00	0.53	-3.92	cool
432		-11.72	-2.36	14.26	11.85	10.30	>12.73	2.41	1.55	-3.43	
433		-10.34	-2.53	14.73	12.34	9.38	8.43	2.39	2.96	0.95	
435		-10.72	-4.41	13.27	11.29	9.66	9.23	1.98	1.63	0.43	
437		5.08	-6.75	14.66	12.41	10.85	>12.73	2.25	1.56	-2.88	
438		-9.96	-8.32	13.89	11.81	10.78	>12.73	2.07	1.04	-2.95	
439		-10.25	-8.80	13.09	11.50	10.28	10.11	1.59	1.22	0.17	
440		-10.66	-8.35	14.01	11.93	10.81	>12.73	2.08	1.12	-2.92	
441	IRS 14NE	-2.20	-9.19	11.84	9.43	7.71	7.87	2.41	1.72	-0.16	cool
461		-4.20	1.85	14.02	11.44	9.47	9.77	2.58	1.97	-0.30	
462		-0.83	-4.95	15.90	13.66	9.48	10.27	2.23	4.18	-0.79	
464		3.89	-7.63	15.32	13.14	10.85	>12.73	2.18	2.29	-2.88	
465		-8.47	-10.46	>12.73	11.63	10.43	10.85	2.11	1.20	-0.42	
488	IRS 1C	4.05	-0.22	12.62	10.42	8.50	8.54	2.20	1.92	-0.04	
490		-9.24	3.69	14.48	12.03	10.58	10.59	2.45	1.45	-0.02	
491		-2.37	-1.44	15.16	12.88	10.38	>12.73	2.28	2.50	-3.35	
492	IRS 21	-0.58	-3.80	14.01	10.41	6.29	5.47	3.61	4.12	0.82	red
498		-8.91	-4.03	14.16	11.43	10.05	9.56	2.73	1.38	0.49	
500		-9.48	-8.30	14.00	12.09	11.33	11.34	1.91	0.77	-0.02	
501		-3.21	-8.25	14.20	12.17	10.64	>12.73	2.03	1.53	-3.09	
502		-3.59	-8.36	13.71	11.26	10.21	10.98	2.45	1.05	-0.77	
503		-5.05	-10.21	12.93	10.65	9.03	9.32	2.28	1.62	-0.29	
523		-6.76	0.58	>20.34	15.07	9.66	8.80	6.27	5.41	0.87	
524		-6.08	0.67	15.09	12.93	9.80	>12.73	2.17	3.13	-3.93	
525	IRS 29NE	-3.90	1.15	14.61	11.57	8.91	8.53	3.04	2.66	0.38	
527		-11.21	-3.72	14.33	12.03	10.74	11.35	2.31	1.29	-0.61	

Table 1: continued

ID	Name	$\Delta\alpha(^{\circ})$	$\Delta\delta(^{\circ})$	<i>H</i>	<i>K</i>	<i>L</i>	<i>M</i>	$(H - K)_{\text{obs}}$	$(K - L)_{\text{obs}}$	$(L - M)_{\text{obs}}$	Notes
528		-11.96	-4.24	13.71	11.91	10.51	10.34	1.80	1.40	0.17	
529		1.85	-6.73	13.80	11.80	9.92	>12.73	2.00	1.89	-3.81	
530		2.50	-7.03	13.62	11.65	8.34	7.51	1.96	3.31	0.84	
531		1.71	-9.29	14.96	12.86	10.07	>12.73	2.10	2.79	-3.66	
532		-11.74	-6.16	14.52	12.55	11.03	10.45	1.96	1.52	0.58	
533		-12.10	-6.58	12.37	10.57	9.25	9.05	1.80	1.32	0.20	
534	IRS 12S	-6.57	-9.54	12.07	10.03	8.31	8.91	2.04	1.73	-0.61	cool
535		2.21	-10.53	14.97	12.83	10.64	>12.73	2.14	2.19	-3.09	
549		-11.94	-10.03	14.76	12.77	10.35	10.56	1.98	2.42	-0.21	
567		-5.29	5.10	15.24	12.90	11.31	10.02	2.34	1.58	1.29	
568		1.44	2.20	14.93	12.99	10.06	>12.73	1.94	2.93	-3.67	
569	IRS 35	0.07	-2.23	14.55	11.80	8.63	9.00	2.75	3.17	-0.37	
570		4.06	-1.31	12.95	10.45	8.53	8.91	2.49	1.93	-0.39	
571	IRS 1SE	4.65	-1.59	12.47	10.48	8.78	>12.73	1.99	1.71	-4.95	cool
574		5.25	4.63	15.35	13.20	10.96	>12.73	2.14	2.24	-2.76	
580		6.14	-0.71	>20.34	12.65	9.95	9.14	8.70	2.70	0.81	
581		6.63	-0.89	>20.34	12.47	10.62	9.86	8.87	1.85	0.76	
582		-2.86	-4.37	15.98	13.71	9.85	>12.73	2.27	3.86	-3.88	
584		2.62	-9.35	13.81	11.36	9.40	8.62	2.45	1.96	0.77	
588		-6.64	-8.51	12.58	10.61	9.04	9.04	1.97	1.58	-0.01	
610		-11.49	-7.01	13.39	11.67	10.49	10.18	1.72	1.18	0.31	
612		-5.35	-9.60	13.78	11.74	10.93	11.10	2.04	0.80	-0.16	
617		-2.93	-10.87	15.79	12.80	10.51	11.04	2.99	2.29	-0.53	
626		2.24	3.59	>20.34	13.05	9.05	8.16	8.30	4.00	0.89	
628	IRS 1NEE	4.87	0.45	12.76	10.56	9.23	9.57	2.19	1.34	-0.34	
629		-6.61	0.97	14.28	11.81	8.87	8.32	2.48	2.94	0.55	
630	IRS 34	-7.01	0.77	14.64	11.32	8.23	7.62	3.32	3.09	0.61	He I
631	IRS 33SE	-2.33	-4.13	11.97	9.95	8.17	8.03	2.02	1.78	0.13	
633		-2.23	-5.09	13.87	11.94	10.38	>12.73	1.92	1.57	-3.35	
635		1.07	-5.84	14.16	11.81	10.20	>12.73	2.35	1.61	-3.53	
636		-1.22	-7.39	12.90	10.79	9.63	10.25	2.11	1.16	-0.62	
637	AF/AHH	-9.68	-7.81	12.46	10.43	8.70	8.10	2.03	1.72	0.60	He I
638		-0.50	-8.80	14.37	11.90	10.53	>12.73	2.46	1.38	-3.20	
647	IRS 7	-2.80	4.63	10.32	8.77	4.48	4.30	1.56	4.28	0.18	cool M2 I
650	IRS 6E	-8.16	-0.07	12.57	9.58	6.34	5.71	3.00	3.24	0.62	WC9
651	IRS 6W	-10.75	0.61	12.33	10.19	7.83	6.84	2.14	2.36	0.98	
655	IRS 1NE	4.22	0.73	12.59	10.28	8.52	8.72	2.31	1.76	-0.20	cool
658		4.65	4.99	16.53	14.10	10.71	>12.73	2.42	3.39	-3.02	
661		-1.25	-1.62	14.93	12.83	8.86	8.42	2.10	3.96	0.45	
662	IRS 16SWE	-1.08	-2.17	13.45	10.67	7.70	7.12	2.78	2.97	0.57	
663		-1.51	-8.26	14.02	12.03	10.43	>12.73	1.99	1.60	-3.30	
669		4.67	1.73	15.63	13.41	11.31	9.87	2.21	2.10	1.45	
670		-2.88	-1.06	15.56	12.93	10.62	>12.73	2.63	2.31	-3.11	
671		-1.69	-2.92	12.52	10.34	8.54	7.94	2.18	1.80	0.60	
672		-1.33	-3.91	14.08	11.84	9.54	>12.73	2.24	2.30	-4.19	
674		0.28	-3.77	15.00	12.43	10.72	>12.73	2.56	1.71	-3.01	
675		0.17	-5.96	14.22	12.09	8.64	8.37	2.13	3.45	0.27	
676		1.31	-8.36	16.17	13.90	9.10	7.91	2.27	4.80	1.19	
677		-4.83	-7.43	13.61	11.36	9.72	10.05	2.24	1.64	-0.33	
679		2.91	5.08	17.54	13.92	10.39	>12.73	3.61	3.53	-3.34	
680		5.43	3.25	13.48	11.29	9.72	>12.73	2.19	1.57	-4.01	
681	IRS 1SW	3.50	-0.84	12.73	10.43	7.33	6.54	2.30	3.10	0.79	
690		-3.38	-3.06	17.28	14.68	8.95	8.54	2.61	5.73	0.40	
691		0.68	-7.04	17.28	>17.66	9.20	8.40	-1.37	9.46	0.81	
694		-2.87	3.34	16.79	14.05	9.39	>12.73	2.74	4.66	-4.34	

Table 1: continued

ID	Name	$\Delta\alpha(^{\circ})$	$\Delta\delta(^{\circ})$	<i>H</i>	<i>K</i>	<i>L</i>	<i>M</i>	$(H - K)_{\text{obs}}$	$(K - L)_{\text{obs}}$	$(L - M)_{\text{obs}}$	Notes
697	IRS 1W	2.43	-0.50	11.73	8.90	4.92	4.02	2.83	3.98	0.90	red
698	IRS 16NE	0.00	0.00	10.68	9.18	7.16	6.87	1.49	2.03	0.29	He I
702	IRS 10W	3.75	4.07	12.95	9.86	6.25	5.02	3.09	3.61	1.23	
704		1.60	4.26	13.60	11.34	9.11	>12.73	2.26	2.23	-4.62	
705		-9.65	2.04	17.36	14.52	9.75	>12.73	2.84	4.77	-3.98	
710		-0.06	-1.12	14.77	12.34	9.11	>12.73	2.42	3.23	-4.62	
711	IRS 33SW	-3.35	-4.20	12.73	10.69	8.61	8.65	2.05	2.08	-0.04	
715		-2.75	5.53	15.77	14.50	10.66	>12.73	1.27	3.84	-3.07	
716		-0.27	-5.51	17.44	>17.66	10.05	8.66	-1.22	8.61	1.39	
718		0.83	-8.37	13.85	11.69	9.15	8.40	2.16	2.53	0.75	
720		-7.01	-6.46	14.38	11.60	7.63	6.54	2.78	3.97	1.10	
721		0.70	-6.36	17.47	15.65	9.24	>12.73	1.82	6.41	-4.49	
723	IRS 7SE	-0.61	3.52	13.38	11.20	10.32	10.22	2.18	0.88	0.10	
724		2.94	1.13	14.29	12.07	9.91	>12.73	2.22	2.16	-3.82	
725		2.98	-1.05	13.77	11.16	7.34	6.91	2.60	3.82	0.43	
728		-9.00	-1.92	16.49	14.16	9.80	8.94	2.32	4.36	0.86	
729		-10.41	-0.68	15.45	13.27	10.12	>12.73	2.18	3.15	-3.61	
730		0.84	5.61	15.56	13.64	11.10	9.77	1.92	2.54	1.33	
731		-4.56	-1.45	14.23	12.32	9.94	9.22	1.91	2.38	0.72	
733		-2.25	-2.60	13.03	11.10	8.56	>12.73	1.94	2.54	-5.17	
737		-1.41	3.69	14.42	11.55	9.87	10.44	2.87	1.68	-0.57	
739		-3.85	6.78	13.08	11.37	9.65	9.50	1.71	1.72	0.15	
741		-3.81	-2.53	13.46	11.24	9.25	9.03	2.23	1.99	0.21	
742		-6.70	-4.24	18.79	15.40	8.00	>12.73	3.39	7.41	-5.73	
743		-3.25	-7.10	13.10	10.80	9.26	9.10	2.29	1.54	0.16	
744		2.21	-8.21	13.61	11.64	9.92	9.45	1.96	1.72	0.48	
745		1.00	6.24	>20.34	11.02	8.91	7.94	10.33	2.10	0.97	
748		4.64	3.92	16.00	13.50	10.07	>12.73	2.50	3.43	-3.66	
751		-7.07	-2.98	13.68	10.89	7.97	8.00	2.78	2.92	-0.03	
752		4.34	5.72	15.22	13.39	10.90	>12.73	1.83	2.49	-2.83	
753		-1.87	4.89	13.74	11.17	9.48	10.02	2.56	1.69	-0.54	
754		1.64	0.69	16.12	14.20	9.85	>12.73	1.92	4.34	-3.87	
755		-4.57	-3.82	13.52	11.57	9.32	9.66	1.95	2.25	-0.34	
757		1.22	-9.13	14.82	12.40	9.70	>12.73	2.42	2.70	-4.03	
759		-5.80	4.61	14.80	12.41	10.48	>12.73	2.39	1.93	-3.25	
760		-3.83	-1.96	15.76	13.42	10.77	>12.73	2.34	2.64	-2.95	
761		0.49	-1.57	15.26	12.97	9.62	>12.73	2.29	3.36	-4.11	
763		1.13	-7.82	15.08	13.23	9.33	>12.73	1.86	3.90	-4.40	
769		-6.06	-1.82	16.69	13.61	7.36	6.55	3.08	6.24	0.82	
772		0.17	2.45	15.37	12.26	9.77	>12.73	3.11	2.49	-3.96	
774		-4.29	-1.21	14.07	12.19	10.23	9.80	1.88	1.96	0.42	
775		-6.35	-3.78	18.20	15.06	7.57	7.19	3.15	7.49	0.38	
776		-7.51	-7.51	17.26	15.08	9.81	>12.73	2.17	5.27	-3.92	
778		-1.25	5.56	15.84	12.87	11.03	11.16	2.96	1.85	-0.13	
779		-5.23	1.94	18.21	14.82	8.95	>12.73	3.39	5.87	-4.77	
781	IRS 2S	-6.75	-5.61	12.83	10.18	7.92	7.53	2.65	2.26	0.38	cool
782	IRS 20	-3.92	-6.23	12.54	10.57	8.70	8.61	1.97	1.87	0.09	cool
784		2.60	1.98	13.72	11.68	9.79	9.53	2.04	1.89	0.27	
785		-8.54	1.74	19.78	>17.66	9.57	8.25	1.12	9.09	1.32	
786	IRS 16SW	-1.87	-1.97	11.53	9.80	7.92	7.53	1.74	1.88	0.39	He I
791		-6.30	3.04	17.92	16.14	9.28	>12.73	1.77	6.86	-4.44	
792		-8.95	-1.41	17.42	14.36	10.06	8.96	3.06	4.30	1.11	
820	IRS 3	-5.24	2.91	14.98	10.64	4.84	3.35	4.35	5.8	1.49	red
825	IRS 10E*	4.94	3.11	13.62	9.76	5.95	5.20	3.86	3.81	0.75	
828		1.21	1.48	17.09	14.82	10.63	>12.73	2.26	4.20	-3.10	

Table 1: continued

ID	Name	$\Delta\alpha(^{\circ})$	$\Delta\delta(^{\circ})$	<i>H</i>	<i>K</i>	<i>L</i>	<i>M</i>	$(H - K)_{\text{obs}}$	$(K - L)_{\text{obs}}$	$(L - M)_{\text{obs}}$	Notes
829		0.88	0.60	14.54	12.10	9.20	8.31	2.44	2.90	0.89	
830		0.76	-0.01	15.29	12.81	9.56	8.58	2.48	3.26	0.98	
831		1.02	-0.79	17.14	14.91	9.78	>12.73	2.22	5.13	-3.94	
833		-9.26	0.70	18.19	15.86	9.61	>12.73	2.33	6.25	-4.12	
836		-8.89	-0.81	16.75	14.26	9.88	>12.73	2.50	4.38	-3.85	
838		-5.62	-2.32	>20.34	13.26	8.16	7.07	8.09	5.09	1.09	
839	IRS 13E	-6.18	-2.49	12.16	9.02	6.18	5.73	3.13	2.84	0.45	He I
840		-5.93	-2.63	11.90	>17.66	7.19	6.63	-6.76	11.47	0.56	
841		-7.31	-2.48	14.21	12.26	8.86	8.73	1.95	3.41	0.12	
845		-5.69	-4.65	16.57	14.01	8.82	>12.73	2.56	5.19	-4.91	
846	IRS 2L	-6.47	-4.82	14.26	10.60	6.49	5.55	3.67	4.11	0.94	
848		-4.98	-5.19	16.53	14.32	9.33	8.60	2.21	4.99	0.73	
849		-5.54	-5.32	16.83	14.61	8.77	7.80	2.21	5.84	0.97	
851		-4.20	-5.23	>20.34	16.04	9.66	9.24	5.31	6.38	0.42	
852		-4.76	-5.87	15.58	13.47	9.15	>12.73	2.11	4.33	-4.58	
856		-2.93	-5.84	15.69	13.63	10.34	>12.73	2.06	3.29	-3.39	
857		-3.57	-6.47	14.37	12.33	9.90	>12.73	2.04	2.43	-3.83	
864		1.69	3.96	15.03	12.39	>14.47	8.69	2.64	-3.08	6.77	
865		1.57	-0.87	14.83	13.00	>14.47	8.92	1.83	-2.47	6.54	
866		0.28	-1.07	14.91	12.48	>14.47	9.09	2.42	-2.98	6.38	
867		-11.30	-0.91	16.28	14.12	>14.47	9.06	2.17	-1.35	6.41	
868		-0.90	-1.61	13.81	11.48	>14.47	8.62	2.33	-3.99	6.85	
869		-5.81	-3.74	14.60	12.11	>14.47	7.73	2.48	-3.36	7.74	
870		-4.51	-5.76	14.53	12.27	>14.47	8.88	2.26	-3.19	6.59	
871		1.49	-7.91	17.80	15.11	>14.47	8.84	2.68	-0.36	6.62	
874		-8.65	-0.90	17.28	14.73	>14.47	9.68	2.55	-0.74	5.79	
876		-5.66	1.93	16.15	13.94	>14.47	8.96	2.22	-1.53	6.51	
877		2.51	-1.02	15.05	12.36	>14.47	7.54	2.70	-3.11	7.93	
878		-7.11	-3.55	16.93	15.32	>14.47	8.36	1.62	-0.15	7.11	
879		1.10	-6.90	15.70	13.78	>14.47	8.77	1.92	-1.69	6.70	
880		-7.27	-8.02	15.33	13.12	>14.47	9.55	2.21	-2.35	5.91	
881		-6.63	2.72	17.23	14.93	>14.47	8.11	2.30	-0.54	7.36	
882		1.38	0.32	16.97	15.19	>14.47	8.84	1.78	-0.28	6.63	
884		-8.58	-2.16	15.11	12.66	>14.47	9.56	2.45	-2.81	5.91	
886		-2.59	-4.35	14.40	12.21	>14.47	9.77	2.19	-3.26	5.69	
887		-7.44	-6.89	16.99	14.79	>14.47	8.63	2.20	-0.68	6.84	
888		-6.79	-9.56	13.30	11.08	>14.47	10.46	2.22	-4.39	5.01	
890		-2.62	-3.51	15.78	14.40	>14.47	8.34	1.38	-1.07	7.13	
892		2.21	3.05	17.36	15.11	>14.47	8.44	2.25	-0.36	7.02	
893		-3.88	-1.62	16.56	14.85	>14.47	10.49	1.71	-0.62	4.98	

Table 2: Photometry of sources outside the NAOS/CONICA field of view

ID	$\Delta\alpha(^{\circ})$	$\Delta\delta(^{\circ})$	<i>L</i>	<i>M</i>	$(L - M)_{\text{obs}}$
1	-0.02	35.63	9.58	9.93	-0.35
3	-5.29	32.78	10.30	10.65	-0.35
4	-22.54	33.76	9.28	9.51	-0.23
5	24.42	32.32	9.61	10.06	-0.45
7	-8.24	31.64	8.96	9.32	-0.36
8	13.29	29.11	9.71	10.06	-0.35
9	17.07	13.60	10.38	10.97	-0.59
10	-25.77	-0.17	9.93	10.39	-0.47
11	23.14	-10.29	9.93	10.25	-0.31
12	2.34	-11.24	9.46	9.38	0.08
14	27.03	-18.73	10.59	11.09	-0.51
15	-25.28	-25.10	10.64	11.01	-0.37
16	-22.50	-27.16	7.49	7.46	0.04
18	-3.17	36.47	8.35	8.55	-0.19
19	27.77	33.51	10.72	11.20	-0.48
20	-0.08	34.14	9.12	9.53	-0.41
23	-33.84	32.93	9.17	9.69	-0.52
24	-4.42	31.34	9.52	9.54	-0.01
25	-22.26	30.09	8.54	8.76	-0.23
28	18.05	25.41	9.70	9.99	-0.29
29	-29.77	23.60	7.66	7.93	-0.27
30	14.63	21.12	10.01	10.24	-0.23
31	-25.89	21.16	7.90	8.04	-0.14
32	-36.30	21.40	9.15	9.77	-0.62
36	-26.57	19.16	9.23	9.44	-0.21
38	5.04	17.33	9.01	9.09	-0.09
39	-4.22	16.46	8.53	8.59	-0.07
40	-19.59	17.13	10.24	10.25	-0.01
41	-19.76	15.10	8.35	8.63	-0.28
42	-38.36	14.80	9.38	9.79	-0.41
43	3.20	13.79	8.87	9.20	-0.33
44	-32.51	12.76	10.51	11.05	-0.53
45	-35.02	11.05	9.27	9.76	-0.49
47	10.37	9.59	8.36	7.29	1.07
48	-33.23	7.74	8.83	9.02	-0.19
49	17.42	5.13	10.62	10.97	-0.35
51	17.84	3.86	9.50	9.84	-0.34
52	-13.61	2.89	9.96	9.91	0.05
53	17.89	1.93	9.14	9.47	-0.33
54	-33.00	1.67	9.45	9.87	-0.42
55	12.49	-1.78	10.56	11.07	-0.52
57	25.23	-7.03	9.66	9.95	-0.29
58	14.12	-7.76	10.60	11.19	-0.59
60	23.98	-9.03	9.66	9.90	-0.25
61	-24.53	-10.02	10.33	10.65	-0.32
62	16.47	-11.64	9.99	10.38	-0.39
63	33.26	-12.39	9.51	9.86	-0.35
64	18.41	-13.38	10.07	10.52	-0.44
65	-22.71	-13.90	10.42	10.63	-0.21
66	10.99	-17.37	10.35	11.16	-0.81
67	29.62	-14.17	9.51	9.85	-0.34
68	-12.15	-15.74	9.44	9.63	-0.19
69	24.60	-14.69	9.45	9.82	-0.36
70	2.68	-15.54	9.68	10.33	-0.65

Table 2: continued

ID	$\Delta\alpha(^{\circ})$	$\Delta\delta(^{\circ})$	<i>L</i>	<i>M</i>	$(L - M)_{\text{obs}}$
71	-19.19	-15.94	10.34	10.72	-0.38
72	23.15	-17.55	8.91	9.20	-0.29
73	-32.50	-17.29	9.89	10.22	-0.33
74	-4.43	-20.02	9.91	10.33	-0.42
76	-23.65	-21.25	9.81	10.17	-0.37
77	10.95	-23.19	9.53	10.04	-0.51
79	-3.74	-26.49	9.56	9.92	-0.35
82	25.07	-28.98	10.42	10.62	-0.21
84	-9.49	-32.13	10.27	10.48	-0.21
86	5.16	-33.02	10.25	10.89	-0.64
87	-25.55	-33.40	9.88	10.31	-0.43
88	30.26	-35.49	10.39	10.96	-0.57
89	4.65	-34.95	9.71	10.19	-0.48
93	17.26	27.79	8.63	8.84	-0.22
94	-13.43	24.89	10.51	10.88	-0.37
95	-13.68	24.10	9.05	9.38	-0.33
96	-16.60	20.03	7.62	7.48	0.14
97	23.22	19.41	10.62	10.81	-0.18
98	8.58	-1.75	9.51	9.68	-0.17
99	-15.48	7.47	9.38	9.51	-0.13
100	-28.06	-1.08	9.77	10.14	-0.37
101	-21.11	-2.56	9.96	10.83	-0.87
105	-28.14	-14.91	9.94	10.28	-0.34
106	-33.20	-21.81	9.50	9.90	-0.40
107	26.39	-23.40	9.62	10.05	-0.43
108	-2.09	-28.81	7.92	8.00	-0.08
110	27.84	-33.49	10.06	10.71	-0.65
113	0.14	36.45	10.24	10.66	-0.41
114	1.51	35.89	10.67	11.26	-0.59
116	14.81	33.75	9.76	10.11	-0.35
117	-5.84	34.15	9.98	10.34	-0.36
121	11.14	30.48	10.53	10.81	-0.28
122	12.12	30.22	9.71	9.74	-0.02
123	33.68	29.52	6.35	6.29	0.06
125	13.88	29.72	9.60	9.83	-0.23
126	14.54	28.98	10.69	11.21	-0.51
127	1.32	26.33	10.04	10.29	-0.25
128	2.28	26.18	10.28	10.52	-0.24
129	-9.55	29.10	9.34	9.67	-0.34
131	23.22	24.94	10.44	10.76	-0.32
132	27.82	25.36	10.25	10.62	-0.38
133	24.44	23.30	10.45	10.58	-0.13
134	25.25	22.75	10.56	10.95	-0.40
135	21.36	24.87	10.19	10.50	-0.31
136	-17.57	24.49	10.00	9.91	0.09
137	12.69	24.28	9.37	9.61	-0.24
138	18.14	23.94	9.42	9.66	-0.24
140	0.44	23.35	10.78	10.68	0.10
142	-11.32	23.01	8.84	8.86	-0.01
143	16.35	21.31	9.79	10.05	-0.26
144	6.11	19.47	9.58	9.91	-0.32
145	6.76	21.14	10.23	10.45	-0.22
146	24.78	20.24	9.59	9.97	-0.38
148	-2.50	19.22	9.93	10.25	-0.32
149	14.35	18.70	9.26	9.61	-0.36

Table 2: continued

ID	$\Delta\alpha(^{\circ})$	$\Delta\delta(^{\circ})$	$L$	$M$	$(L - M)_{\text{obs}}$
150	-37.44	19.59	9.78	10.05	-0.27
151	-11.88	18.48	9.75	9.70	0.05
152	-33.03	18.90	8.53	8.73	-0.20
154	-25.92	17.39	10.02	10.50	-0.48
155	-25.73	16.71	8.49	8.74	-0.25
157	-13.82	16.91	9.99	10.14	-0.15
158	28.46	15.67	9.83	9.81	0.03
161	6.71	14.37	10.10	10.29	-0.19
162	9.12	14.17	10.87	11.22	-0.35
163	16.57	12.19	10.11	10.40	-0.29
164	12.43	12.29	9.34	9.67	-0.33
166	9.09	11.60	10.03	10.14	-0.11
168	10.53	11.94	8.67	8.86	-0.19
170	-1.46	10.46	7.09	6.78	0.31
171	-12.33	11.29	7.95	8.08	-0.13
172	-3.29	10.90	8.83	9.10	-0.28
174	-5.04	7.64	8.59	8.68	-0.09
176	-8.49	8.66	8.92	9.29	-0.37
178	-17.60	6.84	8.78	8.67	0.11
180	-33.05	7.00	10.22	10.65	-0.42
184	13.05	3.47	10.78	11.89	-1.11
185	12.63	0.96	10.07	10.32	-0.26
186	-34.85	3.25	9.45	10.02	-0.57
188	23.19	0.32	9.91	10.41	-0.50
189	21.88	0.07	10.40	11.87	-1.47
190	15.32	-0.42	10.65	11.92	-1.27
191	20.00	-1.49	8.97	9.19	-0.22
192	-16.42	-1.86	10.29	11.29	-0.99
193	-16.53	-2.64	9.96	9.93	0.04
194	12.69	-5.56	9.48	9.57	-0.09
195	10.76	-6.34	9.64	9.73	-0.09
201	-9.35	-11.85	10.77	10.48	0.30
203	-33.34	-10.05	9.93	10.34	-0.41
204	22.40	-12.51	9.06	9.38	-0.32
205	-17.24	-13.39	9.94	10.16	-0.22
208	0.50	-12.50	7.79	8.14	-0.34
209	-19.54	-13.13	10.80	11.68	-0.88
210	3.31	-14.02	10.79	12.02	-1.22
211	-0.93	-16.21	8.97	9.19	-0.23
212	-16.15	-14.22	10.26	10.45	-0.19
213	-3.11	-16.20	9.63	10.02	-0.39
214	-32.14	-16.10	9.76	10.14	-0.38
215	-2.60	-18.12	10.44	11.10	-0.65
219	2.33	-19.32	9.45	9.78	-0.33
220	-4.05	-20.36	10.05	10.39	-0.34
221	-23.00	-18.57	9.45	9.75	-0.31
222	17.12	-20.15	9.62	9.99	-0.36
224	-15.50	-19.85	9.41	9.75	-0.34
225	-26.91	-20.76	10.19	10.51	-0.31
226	-9.41	-22.53	8.48	8.51	-0.03
227	-9.74	-22.14	9.48	9.91	-0.43
228	-24.79	-22.45	10.04	10.28	-0.24
231	0.66	-23.28	10.17	10.24	-0.07
232	-5.56	-23.05	10.47	10.73	-0.26
234	26.56	-25.33	9.27	9.65	-0.37

Table 2: continued

ID	$\Delta\alpha(^{\circ})$	$\Delta\delta(^{\circ})$	<i>L</i>	<i>M</i>	$(L - M)_{\text{obs}}$
235	-22.85	-25.24	9.31	9.63	-0.32
236	-1.15	-26.21	10.32	10.58	-0.26
237	-38.85	-25.91	9.41	10.41	-1.00
238	-2.33	-26.55	10.07	10.44	-0.37
239	0.55	-27.68	10.34	10.70	-0.36
240	0.93	-31.02	10.51	10.95	-0.44
241	-5.92	-30.80	10.44	10.88	-0.43
242	-30.11	-30.94	8.95	9.20	-0.25
243	-19.09	-31.23	10.40	10.64	-0.24
244	-8.56	-33.04	10.27	10.55	-0.28
245	-30.87	-33.15	9.78	10.29	-0.51
248	-18.52	-35.56	9.73	10.04	-0.31
250	12.07	34.82	9.35	9.81	-0.47
251	32.39	33.37	7.97	8.20	-0.23
254	2.06	31.25	10.59	10.84	-0.24
257	32.79	28.90	9.55	9.86	-0.31
258	-13.12	25.62	8.82	9.15	-0.33
259	-13.83	25.46	9.65	9.92	-0.28
262	-14.90	25.05	9.88	10.27	-0.40
263	11.82	23.24	9.82	10.14	-0.32
264	-18.96	23.20	7.89	8.05	-0.16
267	-13.35	21.90	10.75	11.74	-1.00
268	19.37	19.10	10.95	11.07	-0.11
269	16.78	17.19	9.73	9.99	-0.26
272	-4.72	12.96	10.24	10.60	-0.36
274	19.08	11.30	10.30	10.86	-0.56
276	13.68	7.76	9.30	9.69	-0.40
278	-2.16	8.33	9.45	9.93	-0.48
279	-2.77	7.68	9.42	9.39	0.03
280	9.29	5.90	10.31	10.99	-0.68
281	-35.04	5.27	9.43	9.94	-0.51
282	10.51	4.38	6.99	7.02	-0.03
283	13.02	4.63	9.83	10.23	-0.40
284	20.56	0.22	10.29	10.62	-0.33
285	7.76	0.04	8.18	8.33	-0.15
289	19.18	-2.40	9.87	10.19	-0.32
291	11.54	-8.24	10.22	10.17	0.05
292	-13.88	-8.94	9.22	9.60	-0.38
293	5.83	-9.73	10.90	11.58	-0.68
294	8.36	-10.23	8.96	9.08	-0.12
296	-24.10	-11.47	10.51	10.60	-0.09
297	25.95	-13.76	10.14	10.53	-0.39
298	25.70	-14.13	10.48	10.88	-0.40
299	-22.03	-13.56	10.44	10.71	-0.27
302	-6.79	-16.75	8.15	8.30	-0.15
304	-8.96	-17.43	9.21	9.17	0.04
305	-9.39	-18.53	9.23	9.56	-0.33
306	-8.27	-20.20	10.20	11.18	-0.99
307	16.01	-18.66	9.60	10.05	-0.45
308	-11.08	-20.18	10.48	10.49	-0.01
309	-34.68	-20.77	9.58	9.92	-0.34
310	12.08	-22.50	9.37	9.91	-0.54
311	-10.85	-24.26	10.82	11.09	-0.27
313	-24.69	-25.40	10.18	10.53	-0.35
314	-9.35	-26.24	10.48	10.78	-0.30

Table 2: continued

ID	$\Delta\alpha(^{\circ})$	$\Delta\delta(^{\circ})$	L	M	$(L - M)_{\text{obs}}$
316	-8.63	-27.87	10.34	10.79	-0.44
317	-33.27	-31.73	9.89	10.16	-0.27
318	-16.83	-35.78	10.26	10.30	-0.04
319	-30.69	-35.56	7.74	7.70	0.04
322	-26.47	34.82	9.10	9.61	-0.51
323	27.85	31.55	10.82	10.67	0.15
324	17.65	27.16	10.44	10.38	0.06
325	-5.61	18.99	9.18	9.24	-0.06
329	8.85	2.61	8.75	9.01	-0.27
332	14.37	-6.20	8.52	8.69	-0.17
333	-27.66	-6.31	9.73	10.41	-0.68
334	17.07	-11.21	9.98	10.20	-0.22
335	-15.80	-11.94	7.75	7.83	-0.09
336	-22.72	-14.87	10.44	10.40	0.04
339	-2.01	-23.02	8.30	8.37	-0.07
340	-27.77	-26.09	10.25	10.66	-0.41
342	-36.23	36.07	9.68	10.22	-0.54
343	2.39	33.38	8.21	8.43	-0.22
344	-20.15	33.04	8.48	8.68	-0.20
346	-20.70	30.38	9.89	10.06	-0.17
350	12.13	23.84	10.31	10.55	-0.25
351	20.49	22.42	7.66	7.84	-0.18
352	-27.42	21.31	10.20	10.65	-0.45
353	-16.25	20.53	10.89	11.31	-0.42
355	3.18	19.18	10.31	10.49	-0.19
356	19.39	17.89	10.91	10.83	0.08
358	-0.73	14.74	9.65	10.04	-0.39
363	6.51	7.01	8.79	7.97	0.82
366	-1.27	10.83	9.96	9.27	0.69
368	-7.11	10.48	9.20	9.43	-0.24
369	17.21	9.80	10.42	10.66	-0.24
371	12.74	8.04	9.55	9.93	-0.39
372	-10.39	8.84	10.64	10.44	0.20
374	-12.21	6.02	10.87	11.74	-0.87
380	-15.93	-5.36	9.67	9.95	-0.28
381	-13.13	-5.51	10.70	10.93	-0.23
384	8.17	-7.88	9.20	9.17	0.02
386	-1.56	-12.39	10.78	10.69	0.09
387	8.28	-11.39	9.87	9.74	0.13
388	-12.97	-12.19	9.85	10.32	-0.48
389	-21.51	-12.73	10.45	10.79	-0.34
390	-10.92	-13.99	10.33	10.91	-0.58
391	-11.43	-14.63	9.47	9.81	-0.34
392	-1.16	-14.98	9.91	10.16	-0.25
393	-1.82	-15.53	10.72	10.91	-0.19
395	-6.03	-18.78	10.94	11.21	-0.27
396	-31.77	-18.34	8.60	8.79	-0.19
397	-11.38	-18.95	10.88	11.97	-1.08
398	-12.21	-20.76	8.54	8.68	-0.14
399	-22.27	-18.74	9.42	9.74	-0.32
400	1.17	-19.78	9.73	10.14	-0.41
401	-13.29	-29.36	9.59	9.97	-0.37
403	-32.11	-30.38	8.98	9.20	-0.21
404	14.24	31.98	10.64	10.86	-0.23
406	0.82	25.80	9.76	10.06	-0.30

Table 2: continued

ID	$\Delta\alpha(^{\circ})$	$\Delta\delta(^{\circ})$	L	M	$(L - M)_{\text{obs}}$
407	-16.23	22.79	9.91	10.24	-0.32
408	-8.23	22.46	10.85	11.59	-0.73
409	-0.88	21.12	9.85	10.04	-0.19
410	0.61	17.67	9.03	9.12	-0.09
411	-11.36	15.26	10.47	10.09	0.38
412	-11.22	12.91	7.13	7.34	-0.21
413	-10.92	12.89	9.08	9.03	0.04
415	-8.84	10.68	10.75	11.37	-0.62
416	-13.09	8.76	9.25	9.47	-0.22
419	9.34	-2.23	9.46	9.83	-0.37
420	-35.35	9.20	9.64	10.12	-0.48
429	-31.13	2.22	10.21	11.12	-0.91
434	-12.77	-3.34	10.18	10.17	0.01
436	27.93	-5.47	10.71	11.23	-0.52
442	14.67	-9.68	9.98	10.49	-0.51
443	-12.38	-9.85	10.39	11.03	-0.64
444	-8.53	-13.54	10.71	10.65	0.06
445	10.27	-14.33	9.77	10.57	-0.80
447	12.19	-17.47	9.73	10.67	-0.94
448	24.69	-19.48	8.87	9.07	-0.20
450	-7.03	-25.10	9.05	9.36	-0.31
454	-7.29	-28.62	8.18	8.39	-0.21
455	-18.30	-31.53	9.60	9.85	-0.25
456	18.67	19.87	8.77	8.87	-0.10
457	-2.95	17.42	10.76	10.79	-0.02
458	12.95	9.32	10.31	10.75	-0.45
459	1.33	-0.09	9.24	8.84	0.40
460	12.82	1.91	10.12	10.45	-0.33
463	-28.82	-5.54	10.28	10.76	-0.47
466	-7.46	-23.25	8.54	8.51	0.03
467	-5.67	-28.77	9.71	10.00	-0.29
469	1.55	33.58	9.37	9.68	-0.30
470	2.74	33.91	10.38	10.57	-0.20
474	-4.26	18.93	9.35	9.51	-0.16
475	-5.13	16.62	10.42	11.00	-0.59
478	5.80	11.81	9.10	9.43	-0.33
479	1.85	10.11	10.66	10.72	-0.06
483	8.14	5.71	9.48	8.91	0.57
486	-2.61	9.40	9.67	9.52	0.15
487	-6.18	8.87	8.81	9.08	-0.27
489	26.64	6.98	9.85	10.33	-0.48
493	-22.32	-1.51	10.31	10.62	-0.32
494	17.85	-3.72	8.71	8.80	-0.09
495	18.79	-3.40	10.52	10.90	-0.39
496	18.14	-4.41	9.65	10.09	-0.45
499	10.02	-7.97	10.66	11.10	-0.44
506	-38.26	-14.45	9.04	9.40	-0.36
507	-12.93	-16.43	9.90	9.91	-0.01
508	14.10	-23.96	10.28	10.93	-0.65
509	-31.21	-28.27	9.28	9.58	-0.30
511	-10.46	-31.71	10.60	10.88	-0.28
512	15.63	27.39	9.89	10.13	-0.24
513	10.75	22.49	8.37	8.62	-0.25
515	-4.49	12.33	10.53	11.09	-0.56
516	4.48	9.03	9.46	9.42	0.04

Table 2: continued

ID	$\Delta\alpha(^{\circ})$	$\Delta\delta(^{\circ})$	<i>L</i>	<i>M</i>	$(L - M)_{\text{obs}}$
517	-4.30	9.21	9.84	9.22	0.61
520	23.48	2.33	8.83	9.00	-0.17
521	15.03	2.42	10.79	10.89	-0.10
526	22.70	-2.19	10.73	11.17	-0.43
536	-9.12	-10.83	9.54	9.86	-0.32
538	7.82	-15.03	9.73	9.98	-0.25
539	11.44	-20.03	7.77	7.94	-0.17
540	-17.83	27.85	9.78	9.94	-0.16
541	5.89	20.15	10.11	10.31	-0.20
542	13.67	9.17	10.33	10.72	-0.39
543	13.54	8.83	9.98	10.36	-0.38
551	12.29	-12.25	7.82	8.02	-0.20
552	-11.89	-12.12	8.85	8.95	-0.10
553	-36.86	-13.97	8.50	8.68	-0.18
554	13.04	-23.34	7.87	7.98	-0.11
555	-1.71	-23.66	8.91	9.08	-0.18
556	-6.81	-25.45	9.07	9.46	-0.39
559	16.62	29.76	10.44	10.89	-0.45
560	1.70	28.06	9.32	9.53	-0.21
562	-15.81	19.23	10.81	10.66	0.15
563	10.64	15.65	10.73	10.05	0.68
564	-2.17	17.05	9.44	9.27	0.17
565	-13.49	13.25	10.68	10.07	0.61
572	-11.53	7.65	10.65	10.52	0.14
576	-17.99	3.44	10.39	10.47	-0.08
577	-18.14	0.63	9.99	10.07	-0.08
583	-12.52	-1.29	9.27	9.15	0.12
586	7.56	-7.09	7.30	7.43	-0.13
587	32.91	-10.06	9.55	9.92	-0.37
589	-25.64	-9.06	10.99	10.80	0.19
592	5.25	-18.40	10.44	10.49	-0.05
593	-37.08	-18.52	8.36	8.08	0.28
596	26.90	26.26	9.31	9.75	-0.45
598	-10.05	19.58	9.71	9.58	0.12
599	4.20	12.27	10.44	10.02	0.42
602	3.21	10.63	9.83	10.10	-0.27
606	11.97	9.27	9.74	10.04	-0.30
607	0.35	-0.65	8.93	8.12	0.81
608	20.50	1.97	9.05	9.13	-0.08
614	14.67	4.26	8.94	9.43	-0.49
615	23.99	1.72	10.00	10.10	-0.11
616	-33.14	-6.46	10.45	10.67	-0.22
618	-32.77	-12.34	9.60	9.93	-0.33
619	-34.81	-12.20	9.38	9.64	-0.26
620	24.33	-23.45	9.75	9.89	-0.15
622	-19.58	28.37	10.22	10.41	-0.19
623	-7.29	24.98	10.48	10.95	-0.47
624	8.35	8.33	9.71	8.76	0.94
625	2.32	4.12	9.93	8.58	1.35
627	-15.97	3.17	10.97	11.05	-0.08
640	1.89	31.98	9.84	10.10	-0.26
643	-8.30	12.85	10.32	10.69	-0.37
645	4.67	11.66	10.56	9.99	0.57
648	14.96	4.21	8.54	8.55	-0.01
653	8.86	-15.74	10.55	11.13	-0.59

Table 2: continued

ID	$\Delta\alpha(^{\circ})$	$\Delta\delta(^{\circ})$	<i>L</i>	<i>M</i>	$(L - M)_{\text{obs}}$
657	20.72	-19.77	8.66	9.05	-0.38
678	-6.22	-27.05	6.67	6.91	-0.24
684	0.79	-21.58	10.59	10.76	-0.17
685	17.78	19.01	9.25	9.43	-0.18
686	19.89	14.06	8.67	9.02	-0.35
687	-3.28	8.90	9.97	10.39	-0.42
692	18.98	-11.26	9.86	9.90	-0.04
693	-18.19	5.33	10.21	10.60	-0.38
699	-2.50	28.93	10.12	9.29	0.83
700	-2.73	28.40	10.22	9.37	0.85
708	-1.20	28.75	7.24	6.00	1.24
709	15.45	1.47	9.76	10.10	-0.34
714	-5.58	10.49	8.91	9.21	-0.31
717	0.29	-7.74	9.60	8.83	0.76
727	-10.32	0.82	8.56	7.04	1.52
734	-3.02	-3.33	8.91	8.00	0.91
735	17.70	29.44	9.28	9.49	-0.21
747	-18.45	6.09	10.26	10.33	-0.07
749	-11.37	-29.74	7.14	7.20	-0.05
750	-0.93	28.97	7.41	5.77	1.64
756	-2.71	-2.96	8.84	8.16	0.68
764	6.11	-19.72	7.95	8.17	-0.21
765	20.41	13.92	8.50	8.81	-0.31
767	-7.94	1.55	10.64	10.11	0.54
768	-8.65	0.65	9.92	8.77	1.15
773	-9.78	1.33	9.79	8.08	1.71
793	11.72	-20.26	6.66	7.04	-0.38
794	-1.59	-31.22	8.26	8.47	-0.22
798	-5.78	2.28	8.97	7.84	1.13
800	-7.13	-30.04	9.93	10.19	-0.26
808	-26.87	23.00	8.16	8.44	-0.28
810	15.03	14.01	9.22	9.55	-0.32
811	5.97	8.80	6.10	5.33	0.78
813	25.47	8.84	8.56	8.87	-0.31
814	24.12	6.71	8.74	9.12	-0.37
819	-5.28	3.06	6.54	3.35	3.19
842	-5.62	-3.44	8.23	7.67	0.56
858	-28.78	-6.02	9.04	9.36	-0.32
859	-18.53	-22.65	8.97	9.24	-0.27
860	-13.26	-27.11	8.66	8.88	-0.23
861	4.67	-29.35	7.70	6.73	0.96
862	-12.01	-32.07	8.45	8.88	-0.43
863	-39.97	-33.65	10.93	9.54	1.39